Quantitative 1H MRI, 19F MRI, and 19F MRS of cell-internalized perfluorocarbon paramagnetic nanoparticles

CONTRAST MEDIA & MOLECULAR IMAGING

Received: 27 February 2010, Revised: 27 April 2010, Accepted: 10 May 2010, Published online in Wiley Online Library: 21 July 2010

(wileyonlinelibrary.com) DOI:10.1002/cmmi.398

Quantitative ^{1}H MRI, ^{19}F MRI, and ^{19}F MRS of cell-internalized perfluorocarbon paramagnetic nanoparticles

Maarten B. Kok[a#], Anke de Vries[a,b#], Desiree Abdurrachim[a], Jeanine J. Prompers[a], Holger Grüll[a,b], Klaas Nicolay[a] and Gustav J. Strijkers[a*]

***In vivo* molecular imaging with targeted MRI contrast agents will require sensitive methods to quantify local concentrations of contrast agent, enabling not only imaging-based recognition of pathological biomarkers but also detection of changes in expression levels as a consequence of disease development, therapeutic interventions or recurrence of disease. In recent years, targeted paramagnetic perfluorocarbon emulsions have been frequently applied in this context, permitting high–resolution ^{1}H MRI combined with quantitative ^{19}F MR imaging or spectroscopy, under the assumption that the fluorine signal is not altered by the local tissue and cellular environment. In this *in vitro* study we have investigated the ^{19}F MR–based quantification potential of a paramagnetic perfluorocarbon emulsion conjugated with RGD–peptide to target the cell–internalizing $\alpha_v\beta_3$–integrin expressed on endothelial cells, using a combination of ^{1}H MRI, ^{19}F MRI and ^{19}F MRS. The cells took up the targeted emulsion to a greater extent than nontargeted emulsion. The targeted emulsion was internalized into large 1–7 μm diameter vesicles in the perinuclear region, whereas nontargeted emulsion ended up in 1–4 μm diameter vesicles, which were more evenly distributed in the cytoplasm. Association of the targeted emulsion with the cells resulted in different proton longitudinal relaxivity values, r_1, for targeted and control nanoparticles, prohibiting unambiguous quantification of local contrast agent concentration. Upon cellular association, the fluorine R_1 was constant with concentration, while the fluorine R_2 increased nonlinearly with concentration. Even though the fluorine relaxation rate was not constant, the ^{19}F MRI and ^{19}F MRS signals for both targeted nanoparticles and controls were linear and quantifiable as function of nanoparticle concentration. Copyright © 2010 John Wiley & Sons, Ltd.**

Keywords: MRI; MRS; molecular imaging; emulsion; fluorine; gadolinium; $\alpha_v\beta_3$; RGD

1. INTRODUCTION

In recent years, numerous targeted MR contrast agents have been developed that can be employed for the molecular detection and characterization of diseases such as cancer (1), atherosclerosis (2) and myocardial infarction (3). Association of MRI contrast agents with a specific target generally is detected by an increase in ^{1}H MRI signal intensity on T_1–weighted scans for paramagnetic contrast agents, or a decrease on T_2/T_2^*-weighted scans for superparamagnetic contrast agents. Since several mechanisms such as compartmentalization, internalization, and processing of the contrast agent by cells after binding may influence the relaxivity of the contrast agent, it is not straightforward to quantify contrast agent concentration from the changes in ^{1}H MRI signal intensity, or from T_1– or T_2-values. Previously we have studied the internalization of $\alpha_v\beta_3$-targeted (RGD) and non-targeted (NT) paramagnetic liposomes by human umbilical vein-derived endothelial cells (HUVECs) and its effect on both the longitudinal and transverse relaxivity (4,5). We have shown that internalization of the targeted contrast agent lowered the longitudinal relaxivity in a concentration-dependent manner, thereby severely complicating quantification. Quantification of the contrast agent concentration, however, could prove essential for successful application in the areas of cell tracking (6–10), MRI monitored drug delivery (11,12) and molecular MRI (1–3).

A class of contrast agents that offers great potential for quantification are the fluorine (^{19}F) based contrast agents. In contrast to the Gd-based agents, for which changes in signal intensity in ^{1}H MRI originate from water protons in close proximity to the paramagnetic center, ^{19}F–based contrast agents can directly be detected by ^{19}F MRI or MRS. A variety of ^{19}F-containing contrast agents have been introduced previously including micelles (13), liposomes (14) and emulsions (15). By combining ^{1}H with ^{19}F imaging, the ^{19}F MR signal can be placed into anatomical context. Additionally, Gd–based contrast-enhanced ^{1}H imaging could enable initial high-resolution detection of contrast agent accumulation, followed by quantification using ^{19}F MRS or ^{19}F

* *Correspondence to: G. J. Strijkers, Department of Biomedical Engineering, Eindhoven University of Technology, PO Box 513, 5600 MB Eindhoven, The Netherlands.*
E-mail: g.j.strijkers@tue.nl

a *M. B. Kok, A. de Vries, D. Abdurrachim, J. J. Prompers, H. Gruell, K. Nicolay, G. J. Strijkers*
Biomedical NMR, Department of Biomedical Engineering, Eindhoven University of Technology, The Netherlands

b *A. de Vries, H. Gruell*
Philips Research Europe, Eindhoven, The Netherlands

\# *These authors contributed equally to this work.*

MRI. Although a considerable number of studies have utilized ^{19}F imaging and ^{19}F MRS of fluorine–containing nanoparticles *in vitro* (16,17) and *in vivo* (18–25), thus far only a limited number of papers have addressed the consequences of cellular association on the ^{19}F signals (18,26,27). For reliable *in vivo* quantification, however, it is necessary to know whether cellular binding and internalization influence the relaxometric properties and the linearity of the MR signals with fluorine concentration.

In this *in vitro* study we therefore have examined the quantification potential of a lipid-based paramagnetic perfluorocarbon emulsion upon internalization by human endothelial cells. A paramagnetic perfluorocarbon emulsion was used containing amphiphilic Gd^{3+}-chelates for detection by ^{1}H MRI, a perfluoro-15-crown-5-ether (PFCE) core for ^{19}F MRI and MRS and fluorescent lipids to follow cellular uptake using confocal laser scanning microscopy. The emulsion was cell-internalized by targeting of the $\alpha_\nu\beta_3$–integrin receptor expressed on the endothelial cells using a cyclic RGD–peptide ligand. Emulsion without the cyclic RGD–peptide served as a control system for nonspecific binding and uptake. The association of contrast agents with the cells was monitored using several techniques including ^{1}H MRI, ^{19}F MRI, ^{19}F MRS, fluorescent activated cell sorting (FACS), confocal laser scanning microscopy (CLSM) and quantitative Gd measurements (ICP-AES).

2. RESULTS

Dynamic light scattering (DLS) revealed an average diameter of approximately 170 nm for both the RGD–conjugated (RGD–emulsion) and nontargeted (NT–emulsion) nanoparticles. After preparation, typical lipid concentrations of about 25 mM in the final emulsion suspension were obtained. To study the effect of Ostwald ripening, a molecular diffusion phenomenon that results in a gradual growth of the larger particles at the expense of smaller ones, repeated DLS measurements were performed over a period of 80 days (Fig. 1A). After 80 days, a small increase of about 10 nm in average particle diameter was observed. The polydispersity index (PDI) was found to be 0.10 for both emulsion types at all time points. Figure 1(B, C) shows cryo-TEM images of the RGD- and NT–emulsions, respectively. The cryo-TEM images revealed spherical particles with a dark core, typical for PFCE-filled emulsions. The suspension contained essentially no liposomes. Proton longitudinal and transverse relaxivity at 6.3 T and room temperature were $r_{1,H} = 7.4 \pm 0.1\ \text{mM}^{-1}\,\text{s}^{-1}$ and $r_{1,H} = 8.0 \pm 0.2\ \text{mM}^{-1}\,\text{s}^{-1}$, and $r_{2,H} = 36.8 \pm 0.3\ \text{mM}^{-1}\,\text{s}^{-1}$ and $r_{2,H} = 41.3 \pm 0.2\ \text{mM}^{-1}\,\text{s}^{-1}$ for RGD- and NT-emulsions, respectively.

After incubation of the cells with emulsion, the intracellular localization of the contrast agent was visualized by CLSM by exploiting the rhodamine-PE present in the lipid layer surrounding the hydrophobic PFCE core. Figure 2 shows confocal images of HUVECs incubated with either RGD- or NT–emulsions. The brighter rhodamine–PE fluorescence indicated that the RGD–emulsion was taken up to a higher extent than the NT-emulsion. The fluorescent signal of internalized RGD-emulsion was mainly located in vesicular structures in the perinuclear region. The diameter of these vesicular structures increased from around 1–5 μm after 1 h of incubation to 4–7 μm after 8 h of incubation. After 8 h of incubation with RGD-emulsion, fluorescence was additionally observed throughout the entire cytoplasm. Incubation with NT–emulsion resulted in fluorescent vesicular structures located throughout the entire cytoplasm. The diameter of these fluorescent structures increased from about 1–2 μm after 1 h of incubation to about 3–4 μm after 8 h of incubation. Only minor association of the emulsion with the cellular membrane was observed for incubations with both RGD- and NT-emulsion. For incubation times longer than 3 h the cells appeared smaller than at the beginning and after 8 h some dead cells were observed in the medium, suggesting a mild toxic effect.

Uptake of emulsions was quantified using a combination of techniques, i.e. FACS analysis, absolute gadolinium content determinations as well as ^{19}F MRS. Targeting the $\alpha_\nu\beta_3$-integrin by RGD-peptide resulted in higher uptake of emulsion. Figure 3(A) shows the mean fluorescence intensity (MFI) of rhodamine-PE per cell from FACS analysis as a function of incubation time, which revealed that the MFI of cells with RGD–emulsion was at least a factor of 4 higher than that of cells with NT–emulsion. For pellets of HUVECs incubated with RGD-emulsion, the absolute concentration of gadolinium increased from 0.10 mM after 0.5 h to 0.39 mM after 8 h of incubation (Fig. 3B). Uptake of NT-emulsion was much lower, with gadolinium concentration varying from 0.02 mM after 0.5 h to 0.06 mM after 8 h of incubation. In Fig. 3(C), the ^{19}F MRS PFCE peak area is plotted as a function of incubation

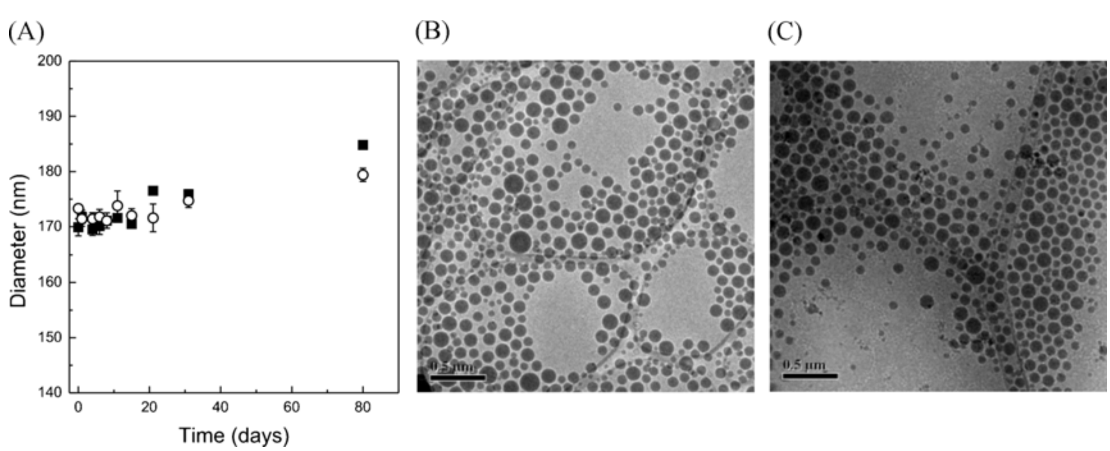

Figure 1. Nanoparticle characterization. (A) Nanoparticle diameter of RGD–emulsion (solid squares) and NT-emulsion (open circles) as function of time after preparation (mean ± SD). (right) Cryo-TEM of (B) RGD–emulsion and (C) NT–emulsion. The scale bar equals 0.5 μm.

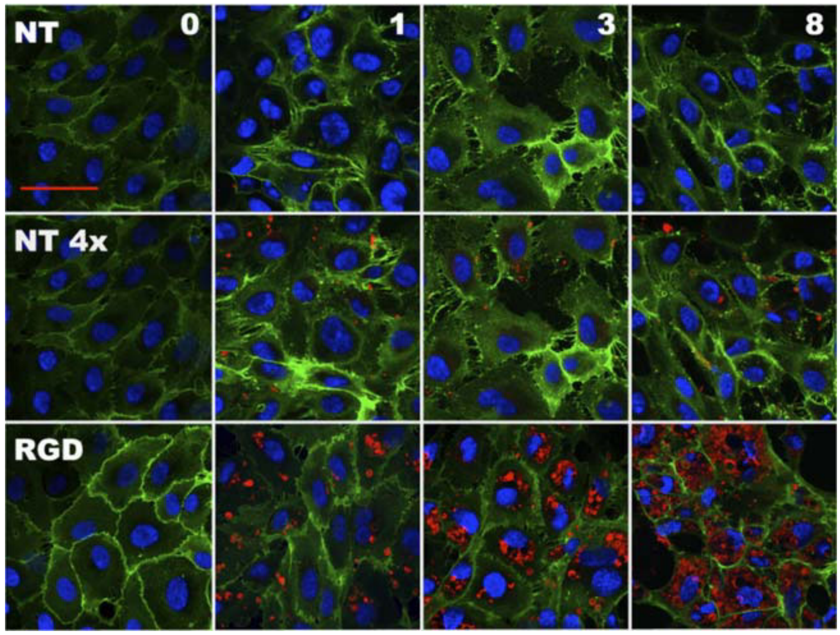

Figure 2. CLSM images of HUVECs incubated with RGD-emulsion (RGD) or NT-emulsion (NT), with green = CD31, red = rhodamine, blue = DAPI. The red scale bar equals 50 μm. The numbers in the top right corners are the incubation times in hours. The laser intensity used to obtain the images labeled NT 4× (middle row) was 4-fold higher than the intensity used to obtain the other images (bottom and top rows).

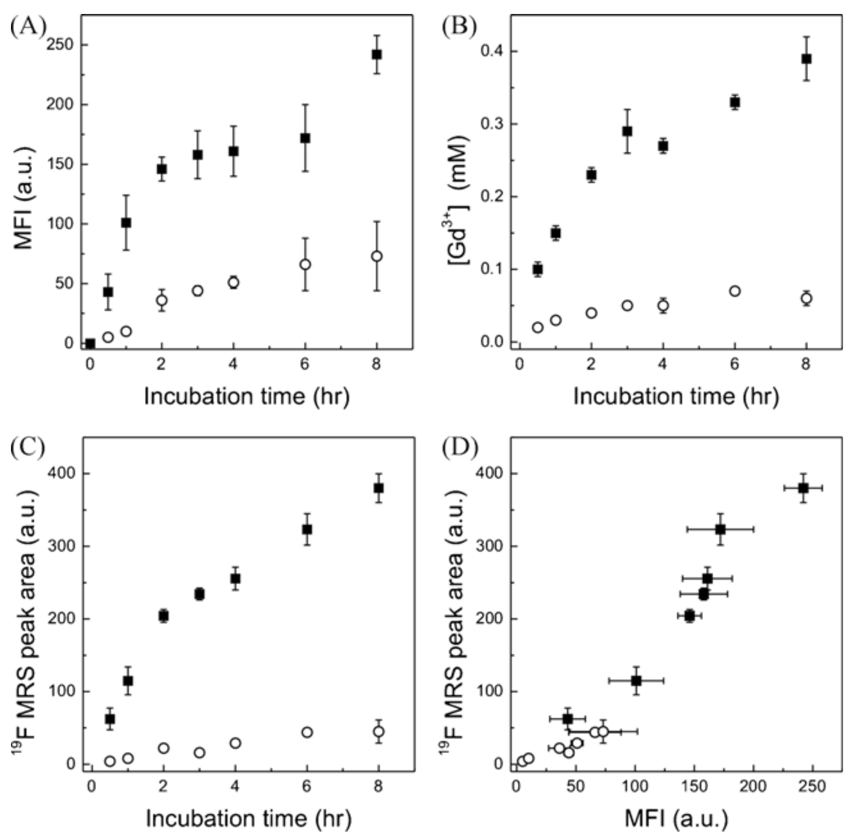

Figure 3. Nanoparticle uptake by HUVEC assessed by FACS, quantitative Gd determinations and ^{19}F MRS for RGD–emulsion (solid squares) and NT–emulsion (open circles). Incubations, varying in time between 0 and 8 h, were performed at an emulsion concentration of 1 μmol total lipid per ml medium. After the incubation the cells were washed to remove nonadherent emulsion nanoparticles. (A) Mean fluorescence intensity per cell (MFI) as function of incubation time. (B) Gadolinium concentration as function of incubation time. (C) ^{19}F MRS peak area as function of incubation time. (D) ^{19}F MRS peak area as function of the mean fluorescence intensity per cell (MFI). Data are means ± SD ($n = 3$).

time. Peak area for HUVECs incubated with RGD–emulsion was at least 6-fold higher than with NT-emulsion for all incubation times. Figure 3(D) shows the correlation between the ^{19}F MRS PFCE peak area and the mean fluorescence intensity.

RGD- and NT-emulsion displayed different proton longitudinal and transversal relaxivities in the cell pellets. Figure 4(A) shows $R_{1,H}$ of the pellets as a function of the gadolinium concentration. For HUVECs incubated with RGD-emulsion, the $R_{1,H}$ increased from a pre-incubation value of 0.49 s^{-1} to 0.87 s^{-1} after 8 h of incubation. For HUVECs incubated with NT-emulsion, $R_{1,H}$ increased from 0.49 to 0.65 s^{-1} with a steeper slope than was the case for incubations with RGD-emulsion. The longitudinal relaxivity ($r_{1,H}$) was determined by linear fittings of $R_{1,H}$ vs the concentration of gadolinium, using the least squared method, resulting in $r_{1,H} = 1.1 \pm 0.1$ and 2.6 ± 0.4 $mM^{-1}\,s^{-1}$ for cells incubated with RGD- and NT-emulsion, respectively. Transverse relaxation rates ($R_{2,H}$) vs the concentration of gadolinium are plotted in Fig. 4(B). For HUVECs incubated with RGD-emulsion $R_{2,H}$ ranged from 28.3 s^{-1} for nonincubated cells to 37.4 s^{-1} for 8 h incubated cells. Incubation of HUVECs with NT–emulsion did not result in a significant change in $R_{2,H}$. The transverse relaxivity ($r_{2,H}$) for RGD–emulsion was determined by linear fitting of the $R_{2,H}$ as a function of the concentration of gadolinium, which resulted in $r_{2,H} = 31 \pm 4$ $mM^{-1}\,s^{-1}$.

The emulsions exhibited different behavior for the fluorine longitudinal and transversal relaxation rates in the cell pellets. Figure 5(A) shows the fluorine longitudinal relaxation rate $R_{1,F}$ as a function of nanoparticle concentration in the cell pellet. $R_{1,F}$ was essentially constant with nanoparticle concentration and equaled the fluorine longitudinal relaxation rate observed for both RGD- and NT-emulsion in aqueous solution (solid line: $R_{1,F} = 1.23 \pm 0.5$ s^{-1}). In sharp contrast, the fluorine transversal relaxation rate in the cell pellets (Fig. 5B) was significantly lower than in aqueous solution (solid line: $R_{2,F} = 74 \pm 1$ s^{-1}) and $R_{2,F}$ increased with increasing nanoparticle concentration.

In order to gain some insight in the structural integrity of the emulsion upon exposure to and internalization in the endothelial cells, the Gd to ^{19}F ratio (nmol μmol^{-1}) was evaluated as a function of the estimated nanoparticle concentration in the cell pellets (Fig. 6). Particularly for low concentrations of NT-emulsion, the Gd to ^{19}F ratio was not constant and was significantly higher than the ratio in the starting material (solid line: Gd/^{19}F $= 0.24 \pm 0.01$).

Linearity of the ^{1}H MRI and ^{19}F MRI contrast-to-noise ratios (CNR), as well as the normalized ^{19}F MRS peak areas with nanoparticle concentration in the cell pellets, which is a premise for absolute quantification, is addressed in Fig. 7. The ^{1}H MRI CNRs for both RGD- and NT-emulsions (Fig. 7A) were fairly linear with nanoparticle concentration ($R^2 = 0.96$ and $R^2 = 0.75$, respectively). However, NT- and RGD-emulsions displayed different slopes, due to different intracellular relaxivity, complicating the distinction between nontargeted and targeted uptake. The ^{1}H MRI detection thresholds were 10.2 and 2.2 nM nanoparticles, or 0.23 and 0.05 mM Gd, for RGD- and NT–emulsions, respectively. The ^{19}F MRI CNR for the RGD-emulsion (Fig. 7B) was quite linear with nanoparticle concentration ($R^2 = 0.97$) in the measured nanoparticle concentration range. For the NT–emulsion the ^{19}F MRI CNR remained below 5 throughout the experiment, however, and therefore could not be determined reliably. The ^{19}F MRI detection threshold for RGD–emulsion was 2.1 nM nanoparticles or 200 mM ^{19}F. Most importantly, the ^{19}F MRS peak area (Fig. 7C), normalized to the pellet volume and corrected for differences in $R_{2,F}$, was highly linear with nanoparticle concentration ($R^2 = 0.99$; data for RGD- and NT–emulsions fitted together). The ^{19}F MRS detection threshold was 0.3 nM nanoparticles or 27 mM ^{19}F.

3. DISCUSSION

In this study we set out to investigate the consequences of cellular internalization on the relaxometric properties and MR quantification potential of a fluorine-containing emulsion. A model system was used, consisting of an *in vitro* culture of human endothelial cells. Cellular internalization was achieved by targeting the cell-internalizing $\alpha_v\beta_3$-integrin receptor with cyclic RGD–peptide. Several readouts ascertained efficient targeting of the RGD-emulsion, in agreement with previous *in vivo* findings (28–30).

As anticipated, quantification using proton MRI proved complex. Although the ^{1}H MRI CNR for RGD– and NT–emulsions were essentially linear with nanoparticle concentrations, the slopes were different for the two emulsion types, hindering

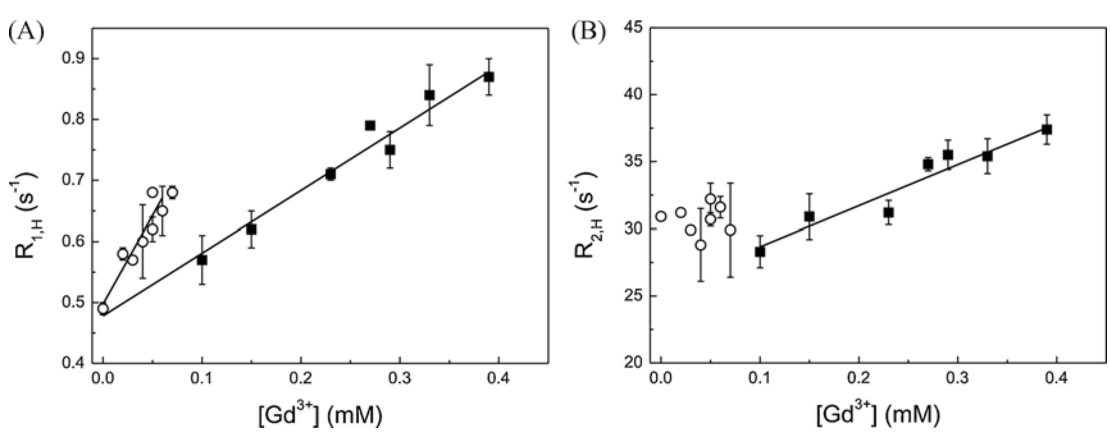

Figure 4. Proton relaxation rates as function of gadolinium concentration in the cell pellets, after incubations with RGD–emulsion (solid squares) or NT–emulsion (open circles). Incubations, varying in time between 0 and 8 h, were performed at an emulsion concentration of 1 μmol total lipid per milliliter medium. After the incubation the cells were washed to remove nonadherent emulsion nanoparticles. (A) Longitudinal proton relaxation rate $R_{1,H}$. Solid lines are linear fits to the experimental data resulting in $r_{1,H} = 1.1 \pm 0.1$ $mM^{-1}\,s^{-1}$ and $r_{1,H} = 2.6 \pm 0.4$ $mM^{-1}\,s^{-1}$ for incubations with RGD- and NT–emulsions, respectively. (B) Transversal proton relaxation rate $R_{2,H}$. The solid line is a linear fit to the experimental data resulting in $r_{2,H} = 31.1 \pm 3.9$ $mM^{-1}\,s^{-1}$ for RGD–emulsion incubated HUVECs. Data are means $\pm$ SD ($n = 3$).

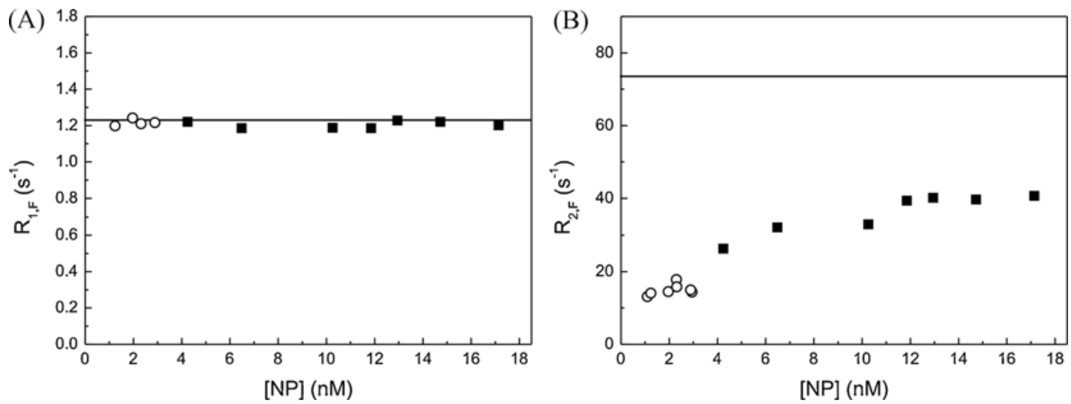

Figure 5. Fluorine relaxation rates as function of nanoparticle concentrations in the cell pellets, after incubations with RGD–emulsion (solid squares) or NT–emulsion (open circles). Incubations, varying in time between 0 and 8 h, were performed at an emulsion concentration of 1 μmol total lipid per ml medium. After the incubation the cells were washed to remove nonadherent emulsion nanoparticles. (A) Longitudinal fluorine relaxation rate $R_{1,F}$. (B) Transversal fluorine relaxation rate $R_{2,F}$. The solid lines are $R_{1,F}$ and $R_{2,F}$ measured for RGD– and NT–emulsions in aqueous solution.

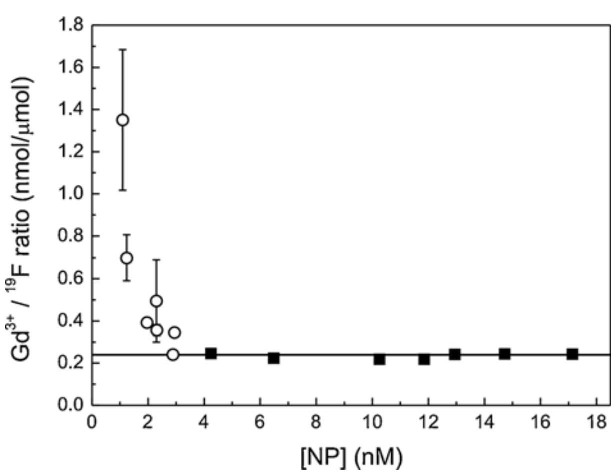

Figure 6. Gadolinium to fluorine ratio (nmol/μmol) as a function of the nanoparticle concentration in the cell pellets for RGD–emulsion (solid squares) and NT–emulsion (open circles). The solid line is the gadolinium to fluorine ratio measured for RGD– and NT–emulsions in acqueous solution. Data are means ± SD ($n = 3$).

unambiguous concentration quantification. The reason for theses different slopes, as a consequence of different longitudinal relaxivities, can be found in the intracellular confinement of the cell–internalized emulsion. NT-emulsion ended up in small 3–4 μm diameter intracellular vesicles, whereas RGD-emulsion was in larger 4–8 μm diameter vesicles. The lower surface to volume ratio of the larger vesicles is associated with a lower water exchange rate across the vesicle membrane, leading to a lower effective relaxivity – an effect coined relaxivity quenching, observed previously for cyclic RGD–conjugated liposomes as well (4,5).

For the fluorine MRI and MRS signals water exchange rates obviously play no role and therefore quantification, i.e. linearity with fluorine concentration, is generally considered straightforward. However, intracellular confinement could still be of importance, when this leads to changes in the fluorine longitudinal and transversal relaxation rates as a result of altered diffusional and translational dynamics or cellular processing and breakdown of the emulsion. Interestingly, we observed that the fluorine longitudinal relaxation rate was not influenced by cellular internalization, whereas the transversal relaxation rate was consistently lower in the cells and concentration-dependent.

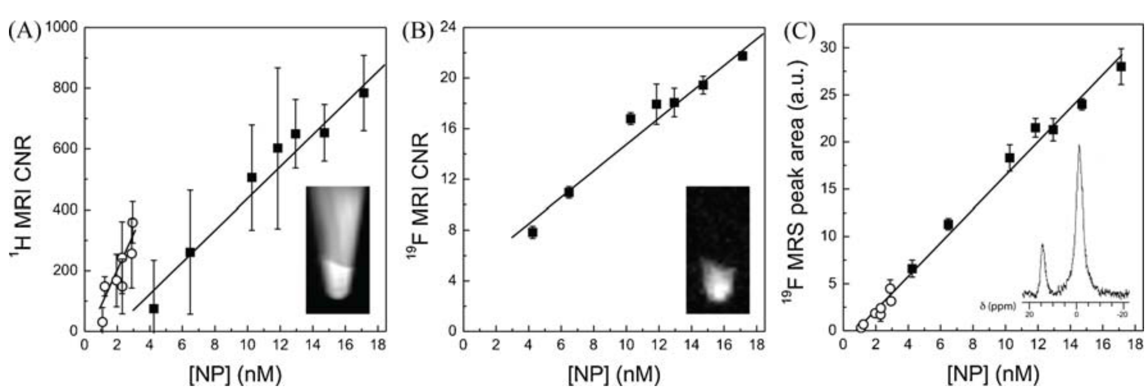

Figure 7. Quantitative proton and fluorine MRI and MRS readouts as function of nanoparticle concentrations in the cell pellets for RGD–emulsion (solid squares) and NT–emulsion (open circles). (A) ^{1}H MRI CNR. The inset is a T_1-weighted ^{1}H MR image of an Eppendorf tube containing a cell pellet with RGD–emulsion. (B) ^{19}F MRI CNR. The inset is a ^{19}F MR image of an Eppendorf tube containing a cell pellet with RGD–emulsion. (C) ^{19}F MRS peak area, normalized to the pellet volume. The inset shows a ^{19}F spectrum with (left) reference TFA peak and (right) perfluoro-15-crown-5-ether peak. Solid lines are linear fits to the data. Data are means ± SD ($n = 3$).

The mechanism responsible for the observed changes in $R_{2,F}$ is not understood, although it seems to be related to the presence of Gd–DOTA–DSPE lipid in the emulsion membrane, as changing $R_{2,F}$ with varying Gd-lipid content in the emulsion membrane was observed previously (31). One could consider a scenario in which the Gd–DOTA–DSPE lipids become separated from the fluorine core by lipid exchange with the cell membrane upon exposure to and internalization into the cells. The emulsion, stripped of Gd–DOTA–DSPE, would exhibit significantly lower transversal relaxation rates because of reduced magnetic susceptibility–induced T_2 shortening, which would be of less influence on the longitudinal relaxation rate, particularly at high magnetic field strength (6.3 T). Moreover, a low pH encountered by the emulsions in the intracellular compartments might trigger release of Gd from the chelate, which could alter the observed relaxation properties. The varying Gd to ^{19}F ratio observed for emulsions in the cells is a strong indicator for the existence of lipid exchange between cell and emulsion. The Gd to ^{19}F ratio deviated from the value found for emulsion in aqueous solution mostly in the low Gd concentration range (Fig. 6), which suggests that this was caused by transfer of Gd–DOTA–DSPE from emulsion to the cells upon initial exposure to the cell culture, rather than originating from differences in Gd and ^{19}F cellular excretion rates. Additionally, Fig. 3(D) shows changing fluorine to fluorescent lipid ratios with higher concentrations of internalized nanoparticles. Another explanation for the initially changing Gd to ^{19}F ratio at low nanoparticle uptake concentrations (Fig. 6) might be found in a preferential uptake of small nanoparticles. Since the smaller nanoparticles have a higher (Gd-containing) surface to (^{19}F–containing) volume ratio, this would also explain the observed initial higher Gd to ^{19}F ratios.

In this paper, the MR quantification potential of nanoparticle concentration was addressed using proton and fluorine MRI as well as fluorine MRS. For ^{1}H MRI and ^{19}F MRI a gradient–spoiled FLASH sequence was used. Although the choice for this sequence was rather arbitrary, both ^{1}H MRI and ^{19}F MRI were performed with near-identical acquisition parameters and the excitation flip angle of the FLASH acquisition was optimized as to yield the best possible signal-to-noise ration (SNR) per unit time, allowing for a fair comparison of the CNRs. The CNR for ^{1}H MRI was highest, although it suffered from a high standard deviation, which was a consequence of variations in baseline SNR between different incubation runs ($n = 3$). ^{19}F MRI has a clear advantage here, since baseline ^{19}F signal is absent. ^{1}H MRI CNR vs nanoparticle concentration resulted in different linear slopes for RGD– and NT–emulsions, prohibiting unambiguous quantification of nanoparticle concentration. Nevertheless, the high CNR and low detection threshold enable high–resolution *in vivo* imaging of nanoparticle distributions in an anatomical context as has been demonstrated in various previous studies (32,33). ^{19}F MRI yielded linear CNR with nanoparticle concentration, which demonstrates that fluorine imaging is quantitative even in the situation when nanoparticles are internalized into cells and exposed to the rather hostile environment of the intracellular space. Changes in the ^{19}F transversal relaxation rates upon internalization should be considered by using an appropriate T_2–insensitive sequence. The ^{19}F MRS normalized peak area was linear with nanoparticle concentration after correction for differences in $R_{2,F}$, with similar slopes for RGD– and NT–emulsions and the detection threshold was lowest. For absolute quantification of nanoparticle concentration the ^{19}F MRI and MRS approaches are most suitable.

In conclusion, we have investigated the changes in proton and fluorine MR relaxometric properties of paramagnetic perfluorocarbon emulsions internalized in human endothelial cells and potential consequences for the MR–based quantification potential of local nanoparticle concentration. For the investigated nanoparticle concentration range (up to approximately 17 nM), proton longitudinal relaxation rates and MRI CNRs were linear with nanoparticle concentration, although different for non-targeted and targeted emulsion types. Upon internalization into the endothelial cells the fluorine longitudinal relaxation rates were found to remain constant, but the fluorine transversal relaxation rate was lower than for emulsion in aqueous solution and increased with increasing nanoparticle concentration. Nevertheless, by using a suitable T_2–insensitive MRI sequence or corrections for differences in fluorine transversal relaxation rates, the fluorine signals were observed to be linear with concentration in the pellets allowing for absolute quantification of nanoparticle concentration.

4. EXPERIMENTAL

4.1. Materials

1,2-Distearoyl-*sn*-glycero-3-phosphocholine (DSPC), cholesterol, 1,2-distearoyl-*sn*-glycero-3-phosphoethanolamine-*N*-[methoxy(-polyethyleneglycol)-2000] (PEG_{2000}-DSPE), 1,2-distearoyl-*sn*-glycero-3-phosphpethanolamine-*N*-[maleimide(polyethyleneglycol)-2000] (Mal-PEG_{2000}-DSPE) and 1,2-dipalmitoyl-*sn*-3-phosphoethanolamine-*N*-[lissamine rhodamine B sulfonyl) (rhodamine-PE) were obtained from Avanti Polar Lipids (Alabaster, AL, USA). 1,2-Distearoyl-*sn*-glycero-3-phosphpethanolamine-[tetraazacyclododecanetetraacetic acid] (Gd–DOTA–DSPE) were synthesized by SyMO-Chem (Eindhoven, the Netherlands) (34). Endothelial growth medium-2 (EGM-2) and human umbilical vein derived endothelial cells (HUVECs) were ordered with Lonza Bioscience (Switzerland). Monoclonal mouse anti-human CD31 antibody was obtained from Dakocytomation (Glostrup, Denmark). Alexa Fluor 488 conjugated goat anti-mouse secondary antibody was from Molecular Probes Europe BV (Leiden, the Netherlands). The cyclic RGD-peptide {c[RGDf(-S-acetylthioacetyl)K]} was synthesized by Ansynth Service BV (Roosendaal, the Netherlands). All other chemicals were obtained from Sigma (St Louis, MO, USA) and were of analytical grade or the best grade available.

4.2. Emulsion preparation and characterization

Emulsions were prepared from perfluoro-15-crown-5-ether (PFCE), Gd–DOTA–DSPE, DSPC, cholesterol, PEG_{2000}-DSPE and Mal-PEG_{2000}-DSPE at a molar ratio of 0.75:1.10:1:0.075:0.075. In detail, 600 μmol total lipids were dissolved in 8 ml 1:5 methanol–chloroform mixture. As a fluorescent marker, 0.1 mol% rhodamine-PE was added. A lipid film was created by evaporating the chloroform–methanol mixture using a Rotavapor R200 (Buchi, Flawil, Switzerland). The lipid film was hydrated at 70°C using a mixture of 4.5 g PFCE and 15 ml THAM buffer, containing 0.0252% w/v trishydroxymethyl aminomethane (THAM) and 8.9 g/l NaCl (pH 7.4). The crude emulsion was homogenized for 30 s using an Ultra-Turrax T8 (IKA-Werke, Staufen, Germany) and subsequently processed for 3 min in a high-pressure microfluidizer (M-110S, Microfluidics, Newton, MA, USA) at 1500 bar, which was preheated to 60°C. The final emulsion was cooled down in an ice bath. After preparation of the emulsion supension, half of the suspension was modified with a cyclic RGD-peptide (6 μg/μmol total lipid) to target the $\alpha_v\beta_3$-integrin. The cyclic RGD-peptide was deacetylated and coupled to the distal end of Mal-PEG2000-DSPE overnight at room temperature. Lipid concentration was measured by phosphate determination according to Rouser *et al*. (35). Size and size-distribution of the emulsions were determined with dynamic light scattering (DLS) (Zetasizer Nano, Malvern, UK) at 25°C. Longitudinal and transverse relaxivity were determined at 6.3 T and room temperature by linear fits of R_1 ($=1/T_1$) and R_2 ($=1/T_2$) values as a function of the gadolinium concentration as determined using inductively coupled plasma atomic emission spectroscopy (ICP-AES). Fluorine content of the emulsion was determined using ion chromatography. The concentration of nanoparticles (NP) was calculated using an estimated 2.25×10^4 Gd-containing lipids per nanoparticle. This value was obtained by dividing the surface area of an emulsion with a diameter of 175 nm by the surface area of a single lipid present in a monolayer (42.5 Å) and taking into account a 1:9 ratio of gadolinium-containing lipids to total lipids. Emulsion was stored for 30 days at room temperature before use in the incubation experiments. In this paper we refer to emulsion conjugated with RGD-peptide as RGD-emulsion. Nontargeted emulsion, which was not conjugated with a targeting ligand, is referred to as NT–emulsion.

4.3. Incubations of HUVEC with emulsions

Human umbilical vein derived endothelial cells were used for all the experiments. Cells were stored in liquid nitrogen upon arrival. Before use, the cells were quickly thawed in a water bath ($T=37$°C) and divided over two gelatin-coated T75 TCPS flasks (VWR, West Chester, PA, USA). Cells were cultured in a humidified incubator at 37°C with 5% CO_2. The EGM-2 medium was replaced every 2–3 days. Cells from passages 3 or 4 were used for all experiments at 80–90% confluency. Incubations were carried out on both gelatin-coated coverslips, for CLSM analysis, and in gelatin-coated T75 TCPS culture flasks, for MRI, FACS and ICP-AES analyses. All measurements were done in triplicate for both types of emulsions and each incubation time. At the start of the experiment, medium was replaced by either RGD-emulsion or NT-emulsion containing medium at a concentration of 1 μmol total lipid per milliliter medium. Four milliliters of emulsion–containing medium was added to the T75 gelatin-coated TCPS flasks and 0.5 ml of medium was added to the gelatin-coated coverslips. The incubation time with emulsion containing medium was varied between 0 and 8 h. After the incubation, cells were washed three times with 5 ml prewarmed (37°C) HEPES-buffered saline solution to remove nonadherent emulsions. After these washing steps, the cells grown on coverslips were fixed using 4% PFA for 15 min at room temperature, washed three times with PBS and subsequently stored in the dark at 4°C. Cells in culture flasks were detached using 2 ml 0.25% w/v trypsin, 1 mM EDTA·4Na (Lonza Bioscience, Switzerland). The trypsin solution was neutralized using 4 ml trypsin neutralizing solution (Lonza Bioscience, Basel, Switzerland). Cells were spun down at 220***g*** and the supernatant was removed and the cell pellet was resuspended in 150 μl 4% paraformaldehyde solution in PBS and transferred to a 300 μl Eppendorf cup. A loosely packed cell pellet was formed by centrifugation at 20***g*** for 5 min The pellets contained in the range of 3–5 million cells. The cell pellets were stored at room temperature in the dark.

4.4. Confocal laser scanning microscopy

After fixation, the coverslips with HUVECs incubated with emulsion were stained using a mouse anti-human CD31 antibody to visualize the cell membrane. The cells were rinsed for 5 min with PBS followed by 60 min of incubation with the primary mouse anti-human CD31 antibody (1:40 dilution). Subsequently the cells were washed for 3×5 min with PBS followed by 30 min of incubation with a secondary Alexa Fluor 488 goat anti-mouse IgG antibody (1:200 dilution). The cells were washed for 3×5 min with PBS and the nuclei were stained for 5 min with DAPI. After staining of the nuclei, the cells were rinsed for 3×5 min with PBS and subsequently mounted on a microscopy slide using Mowiol mounting medium.

Confocal fluorescence images were recorded at room temperature on a Zeiss LSM 510 META system using a Plan-Apochromat® 63 ×/1.4 NA oil-immersion objective. Alexa Fluor 488 and rhodamine-PE were excited using the 488 and 543 nm lines of a HeNe laser, respectively. The fluorescence emission of Alexa Fluor 488 was recorded with photomultiplier tubes (Hamamatsu R6357) after spectral filtering with a NFT 490 nm beamsplitter followed by a 500–550 nm bandpass filter. Rhodamine-PE emission was analyzed using the Zeiss Meta System in a wavelength range of 586–704 nm. DAPI staining of nuclei was visualized by two-photon excitation fluorescence microscopy performed on the same Zeiss LSM 510 system. Excitation at 780 nm was provided by a pulsed Ti:Sapphire laser (Chameleon™; Coherent, Santa Clara, CA, USA), and fluorescence emission was detected with a 395–465 nm bandpass filter. All experiments were combined in multitrack mode and acquired confocally.

4.5. Magnetic resonance imaging and spectroscopy

In this paper we refer to relaxometric properties for proton with subscript H and for fluorine with subscript F. $R_{1,H}$ and $R_{2,H}$ relaxation rates and the volumes of the cell pellets were measured using a 6.3 T horizontal bore animal MR scanner (Bruker BioSpec, Ettlingen, Germany). All measurements were carried out at room temperature. ^{1}H longitudinal and transverse relaxation rates were measured in a 3 cm–diameter send and receive quadrature-driven birdcage coil (Rapid Biomedical, Rimpar, Germany). The Eppendorf tubes containing the loosely–packed cell pellets were placed in a custom made holder (four tubes at a time), which was filled with HEPES-buffered saline solution to facilitate shimming. $R_{1,H}$ was measured using a fast inversion recovery segmented FLASH sequence with an echo time (*TE*) of 1.5 ms, a repetition time (*TR*) of 3.0 ms, a flip angle of 15°, and an inversion time (*TI*) ranging from 67 to 4800 ms in 80 steps. Overall repetition time was 20 s. Field of view (FOV) $=3 \times 2.18\,\text{cm}^2$, matrix size $=128 \times 128$, slice thickness $=0.75$ mm and NSA $=2$. $R_{2,H}$ was measured using a multi-slice multi-echo sequence with *TE* ranging between 9 and 288 ms in 32 steps and $TR=1000$ ms, FOV $=3 \times 2.2\,\text{cm}^2$, slice thickness $=0.75$ mm, matrix size $=128 \times 128$, and NSA $=4$. From the images $R_{1,H}$- and $R_{2,H}$-maps were calculated using Mathematica (Wolfram Research Inc., Champaign, IL, USA). $R_{1,H}$ and $R_{2,H}$ of the cell pellets are reported as the means ± SD of a selected region-of-interest (ROI) within the pellet. The volume of the cell pellet was determined for each sample separately in a 0.7 cm-diameter solenoid coil using a 3D FLASH sequence with $TE=3.2$ ms, $TR=25$ ms, flip angle $=30$°, FOV $=1.6 \times 1.6 \times 1.6\,\text{cm}^3$, matrix size $=128 \times 128 \times 128$ and NSA $=1$. A threshold value was determined manually to select the voxels inside the pellet, which were multiplied by the voxel volume to obtain the total volume of the pellet. The concentration of gadolinium in each cell pellet was determined by dividing the gadolinium content by the pellet volume.

^{1}H MRI, ^{19}F MRI and ^{19}F MRS were performed using a homebuilt 5 mm–diameter solenoid coil, which was tuned to the ^{1}H and ^{19}F resonance frequencies. ^{1}H MRI was performed using a FLASH sequence with $TE = 3.2$ ms, $TR = 100$ ms, flip angle $= 20^\circ$, FOV $= 2.0 \times 2.0$ cm^2, matrix size $= 128 \times 128$, slice thickness $= 2$ mm and NSA $= 128$. Total acquisition time was approximately 10 min ^{19}F MRI was done using a FLASH sequence with $TE = 2.7$ ms, $TR = 100$ ms, flip angle $= 40^\circ$, FOV $= 2.0 \times 2.0$ cm^2, matrix size $= 128 \times 128$, slice thickness $= 2$ mm and NSA $= 128$. As for ^{1}H MRI, the total acquisition time was approximately 10 min. Average signal intensity was determined in a selected ROI within the pellet. ^{19}F MR spectra were obtained using a nonlocalized spectroscopic spin echo sequence with $TE = 2.5$ ms, $TR = 5000$ ms, adiabatic 90° and 180° pulses and two dummy shots. A small sphere containing trifluoroacetic acid (TFA) was used, as a reference for ^{19}F MRS. This sphere was placed next to the Eppendorf cup containing the cell pellet. The number of averages was 8 for HUVECs incubated with RGD–emulsion and 64 for HUVECs incubated with NT-emulsion. The peak intensity and area were determined with the TOPSPIN 1.5 software (Bruker Biospin). Peak area was normalized to the cell pellet volume to account for differences in cell numbers and corrected for $R_{2,F}$. $R_{2,F}$ was determined using the same spectroscopic spin echo sequence by varying the *TE* from 2.5 to 100 ms in 11 steps. $R_{1,F}$ was determined by varying *TR* from 220 to 5000 ms in 11 steps.

4.6. MR detection threshold analysis

Detection thresholds, expressed as the concentration of contrast agent, were determined for ^{1}H MRI and ^{19}F MRI in a circular ROI situated in the cell pellet and for ^{19}F MRS from peak area of the whole pellet. For ^{1}H MRI, CNRs were determined by subtracting the SNR of T_1–weighted images from pellets of nonincubated HUVECs from those of cells incubated with contrast agent. Since nonincubated HUVEC do not contain fluorine, ^{19}F MRI and ^{19}F MRS CNR values were defined with respect to background noise levels (CNR = SNR). Detection thresholds were estimated by determining the minimal contrast agent concentration required to cause a significant change in contrast (CNR > 5), taking into account the standard deviation of measurements using a Student's *t*-test.

Acknowledgements

This study was funded in part by the BSIK program entitled Molecular Imaging of Ischemic Heart Disease (project number BSIK03033) and by the EC-FP6-project DiMI, LSHB–CT–2005–512146. This study was performed in the framework of the European Cooperation in the field of Scientific and Technical Research (COST) D38 Action Metal–Based Systems for Molecular Imaging Applications.

References

1. Weissleder R. Molecular imaging in cancer. Science 2006; 312(5777): 1168–1171.
2. Sanz J, Fayad ZA. Imaging of atherosclerotic cardiovascular disease. Nature 2008; 451(7181): 953–957.
3. Jaffer FA, Sosnovik DE, Nahrendorf M, Weissleder R. Molecular imaging of myocardial infarction. J Mol Cell Cardiol 2006; 41(6): 921–933.
4. Kok MB, Hak S, Mulder WJM, Van der Schaft DWJ, Strijkers GJ, Nicolay K. Cellular compartmentalization of internalized paramagnetic liposomes strongly influences both T_1 and T_2 relaxivity. Magn Reson Med 2009; 61(5): 1022–1032.
5. Strijkers GJ, Hak S, Kok MB, Springer CS Jr, Nicolay K. Three-compartment T_1 relaxation model for intracellular paramagnetic contrast agents. Magn Reson Med 2009; 61(5): 1049–1058.
6. Modo M, Mellodew K, Cash D, Fraser SE, Meade TJ, Price J, Williams SC. Mapping transplanted stem cell migration after a stroke: a serial, in vivo magnetic resonance imaging study. Neuroimage 2004; 21(1): 311–317.
7. Shyu WC, Chen CP, Lin SZ, Lee YJ, Li H. Efficient tracking of non-iron-labeled mesenchymal stem cells with serial MRI in chronic stroke rats. Stroke 2007; 38(2): 367–374.
8. Kustermann E, Roell W, Breitbach M, Wecker S, Wiedermann D, Buehrle C, Welz A, Hescheler J, Fleischmann BK, Hoehn M. Stem cell implantation in ischemic mouse heart: a high-resolution magnetic resonance imaging investigation. NMR Biomed 2005; 18(6): 362–370.
9. Yeh TC, Zhang W, Ildstad ST, Ho C. In vivo dynamic MRI tracking of rat T-cells labeled with superparamagnetic iron-oxide particles. Magn Reson Med 1995; 33(2): 200–208.
10. Brekke C, Williams SC, Price J, Thorsen F, Modo M. Cellular multiparametric MRI of neural stem cell therapy in a rat glioma model. Neuroimage 2007; 37(3): 769–782.
11. Nasongkla N, Bey E, Ren J, Ai H, Khemtong C, Guthi JS, Chin SF, Sherry AD, Boothman DA, Gao J. Multifunctional polymeric micelles as cancer-targeted, MRI-ultrasensitive drug delivery systems. Nano Lett 2006; 6(11): 2427–2430.
12. Viglianti BL, Ponce AM, Michelich CR, Yu D, Abraham SA, Sanders L, Yarmolenko PS, Schroeder T, MacFall JR, Barboriak DP, Colvin OM, Bally MB, Dewhirst MW. Chemodosimetry of in vivo tumor liposomal drug concentration using MRI. Magn Reson Med 2006; 56(5): 1011–1018.
13. Du W, Xu Z, Nystrom AM, Zhang K, Leonard JR, Wooley KL. 19F- and fluorescently labeled micelles as nanoscopic assemblies for chemotherapeutic delivery. Bioconjug Chem 2008; 19(12): 2492–2498.
14. Langereis S, Keupp J, van Velthoven JL, de Roos IH, Burdinski D, Pikkemaat JA, Grüll H. A temperature-sensitive liposomal 1H CEST and 19F contrast agent for MR image-guided drug delivery. J Am Chem Soc 2009; 131(4): 1380–1381.
15. Partlow KC, Lanza GM, Wickline SA. Exploiting lipid raft transport with membrane targeted nanoparticles: a strategy for cytosolic drug delivery. Biomaterials 2008; 29(23): 3367–3375.
16. Morawski AM, Winter PM, Crowder KC, Caruthers SD, Fuhrhop RW, Scott MJ, Robertson JD, Abendschein DR, Lanza GM, Wickline SA. Targeted nanoparticles for quantitative imaging of sparse molecular epitopes with MRI. Magn Reson Med 2004; 51(3): 480–486.
17. Morawski AM, Winter PM, Yu X, Fuhrhop RW, Scott MJ, Hockett F, Robertson JD, Gaffney PJ, Lanza GM, Wickline SA. Quantitative 'magnetic resonance immunohistochemistry' with ligand-targeted (19)F nanoparticles. Magn Reson Med 2004; 52(6): 1255–1262.
18. Kimura A, Narazaki M, Kanazawa Y, Fujiwara H. 19F Magnetic resonance imaging of perfluorooctanoic acid encapsulated in liposome for biodistribution measurement. Magn Reson Imaging 2004; 22(6): 855–860.
19. Srinivas M, Morel PA, Ernst LA, Laidlaw DH, Ahrens ET. Fluorine-19 MRI for visualization and quantification of cell migration in a diabetes model. Magn Reson Med 2007; 58(4): 725–734.
20. Flogel U, Ding Z, Hardung H, Jander S, Reichmann G, Jacoby C, Schubert R, Schrader J. In vivo monitoring of inflammation after cardiac and cerebral ischemia by fluorine magnetic resonance imaging. Circulation 2008; 118(2): 140–148.
21. Srinivas M, Turner MS, Janjic JM, Morel PA, Laidlaw DH, Ahrens ET. In vivo cytometry of antigen-specific t cells using 19F MRI. Magn Reson Med 2009; 62(3): 747–753.
22. Ruiz-Cabello J, Walczak P, Kedziorek DA, Chacko VP, Schmieder AH, Wickline SA, Lanza GM, Bulte JW. In vivo 'hot spot' MR

imaging of neural stem cells using fluorinated nanoparticles. Magn Reson Med 2008; 60(6): 1506–1511.

23. Ahrens ET, Flores R, Xu H, Morel PA. In vivo imaging platform for tracking immunotherapeutic cells. Nat Biotechnol 2005; 23(8): 983–987.
24. Partlow KC, Chen J, Brant JA, Neubauer AM, Meyerrose TE, Creer MH, Nolta JA, Caruthers SD, Lanza GM, Wickline SA. 19F magnetic resonance imaging for stem/progenitor cell tracking with multiple unique perfluorocarbon nanobeacons. FASEB J 2007; 21(8): 1647–1654.
25. Janjic JM, Srinivas M, Kadayakkara DK, Ahrens ET. Self-delivering nanoemulsions for dual fluorine-19 MRI and fluorescence detection. J Am Chem Soc 2008; 130(9): 2832–2841.
26. Janjic JM, Ahrens ET. Fluorine-containing nanoemulsions for MRI cell tracking. Wiley Interdiscip Rev Nanomed Nanobiotechnol 2009; 1(5): 492–501.
27. Venkataramani D, Chen J, Neubauer AM, Crowder Brant J, Lanza GM, Wickline SA. Does endocytosis of perfluorocarbon nanoparticles by progenitor/stem cells alter 19F relaxation at 11.7T? Proc Intl Soc Mag Reson Med 2006; 14: 1890.
28. Winter PM, Caruthers SD, Kassner A, Harris TD, Chinen LK, Allen JS, Lacy EK, Zhang H, Robertson JD, Wickline SA, Lanza GM. Molecular imaging of angiogenesis in nascent Vx-2 rabbit tumors using a novel alpha(nu)beta3-targeted nanoparticle and 1.5 tesla magnetic resonance imaging. Cancer Res 2003; 63(18): 5838–5843.
29. Mulder WJ, Strijkers GJ, Habets JW, Bleeker EJ, van der Schaft DW, Storm G, Koning GA, Griffioen AW, Nicolay K. MR molecular imaging and fluorescence microscopy for identification of activated tumor endothelium using a bimodal lipidic nanoparticle. Faseb J 2005; 19(14): 2008–2010.
30. Schmieder AH, Caruthers SD, Zhang H, Williams TA, Robertson JD, Wickline SA, Lanza GM. Three-dimensional MR mapping of angiogenesis with alpha5beta1(alpha nu beta3)-targeted theranostic nanoparticles in the MDA-MB-435 xenograft mouse model. FASEB J 2008; 22(12): 4179–4189.
31. Neubauer AM, Myerson J, Caruthers SD, Hockett FD, Winter PM, Chen J, Gaffney PJ, Robertson JD, Lanza GM. Wickline SA. Gadolinium-modulated 19F signals from perfluorocarbon nanoparticles as a new strategy for molecular imaging. Magn Reson Med 2008; 60(5): 1066–1072.
32. Mulder WJ, Strijkers GJ, van Tilborg GA, Cormode DP, Fayad ZA, Nicolay K. Nanoparticulate assemblies of amphiphiles and diagnostically active materials for multimodality imaging. Acc Chem Res 2009; 42(7): 904–914.
33. Pan D, Lanza GM, Wickline SA, Caruthers SD. Nanomedicine: perspective and promises with ligand-directed molecular imaging. Eur J Radiol 2009; 70(2): 274–285.
34. Hak S, Sanders HM, Agrawal P, Langereis S, Grüll H, Keizer HM, Arena F, Terreno E, Strijkers GJ, Nicolay K. A high relaxivity Gd(III)DOTA–DSPE-based liposomal contrast agent for magnetic resonance imaging. Eur J Pharm Biopharm 2009; 72(2): 397–404.
35. Rouser G, Fkeischer S, Yamamoto A. Two dimensional thin layer chromatographic separation of polar lipids and determination of phospholipids by phosphorus analysis of spots. Lipids 1970; 5(5): 494–496.